*Article*

# Utilization of Additive Manufacturing for the Rapid Prototyping of C-Band Radiofrequency Loads

Garrett Mathesen [1], Charlotte Wehner [1], Julian Merrick [1], Bradley Shirley [1], Ronald Agustsson [2], Robert Berry [2], Amirari Diego [2] and Emilio Nanni [1,*]

[1] SLAC National Accelerator Laboratory, 2575 Sand Hill Road, Menlo Park, CA 94025, USA; mathesen@slac.stanford.edu (G.M.); julianm@slac.stanford.edu (J.M.); brads@slac.stanford.edu (B.S.)
[2] RadiaBeam, 21735 Stewart Street, Suite A, Santa Monica, CA 90404, USA; agustsson@radiabeam.com (R.A.); berry@radiabeam.com (R.B.); adiego@radiabeam.com (A.D.)
* Correspondence: nanni@slac.stanford.edu

**Abstract:** Additive manufacturing is a versatile technique that shows promise in providing quick and dynamic manufacturing for complex engineering problems. Research has been ongoing into the use of additive manufacturing for potential applications in radiofrequency (RF) component technologies. Here, we present a method for developing an effective prototype load produced from 316L stainless steel on a direct metal laser sintering machine. The model was tested using simulation software to verify the validity of the design. The load structure was manufactured by an online digital manufacturing company, showing the viability of using easily accessible tools to manufacture RF structures. The produced load was able to produce an $S_{11}$ value of $-22.8$ dB at a C-band frequency of 5.712 GHz while under a vacuum. In a high-power test, the load was able to terminate a peak power of 8.1 MW. The discussion includes future applications of the present method and how it will help to improve the implementation of future accelerator concepts.

**Keywords:** direct metal laser sintering; RF load; C band

## 1. Introduction

Advances in additive manufacturing (AM) techniques have led to increased research efforts into their applicability to various engineering challenges and wider adoption within industry. Of particular interest is the ability to use AM technology to simplify the manufacturing process of typically complex parts. This can be exemplified through the research being performed in the aerospace, automotive, and biomedical industries [1]. Research is also being performed to develop engineered solutions for RF components, especially those that require complex geometries such as in the development of terahertz RF structures [2] and X-band klystron and terminating load structures [3,4].

We continued this research by investigating the application of AM techniques for the creation of a C-band load. A background is given on how additive manufacturing works and what design constraints it adds. The motivation for the study included the potential future applications that will require the rapid development of complex high-power loads. A methodology is outlined describing how the simulations and solid models were developed. The results of these simulations along with the results from the tests of the realized spiral load (shown in Figure 1) are shown and discussed.

### 1.1. Background

The process of additive manufacturing can be simplified to the core functionality of laying, binding, or solidifying the layers of a given material on top of one another until a programmed design is produced. This process can be realized through various different mechanical methods, depending mainly on the material chosen. The common AM materials include polymers, ceramics, metals, and composite materials. Within the realm of metal

additive manufacturing (MAM), there are two main methods utilized for realizing MAM parts: direct energy deposit (DED) and powder bed fusion (PBF).
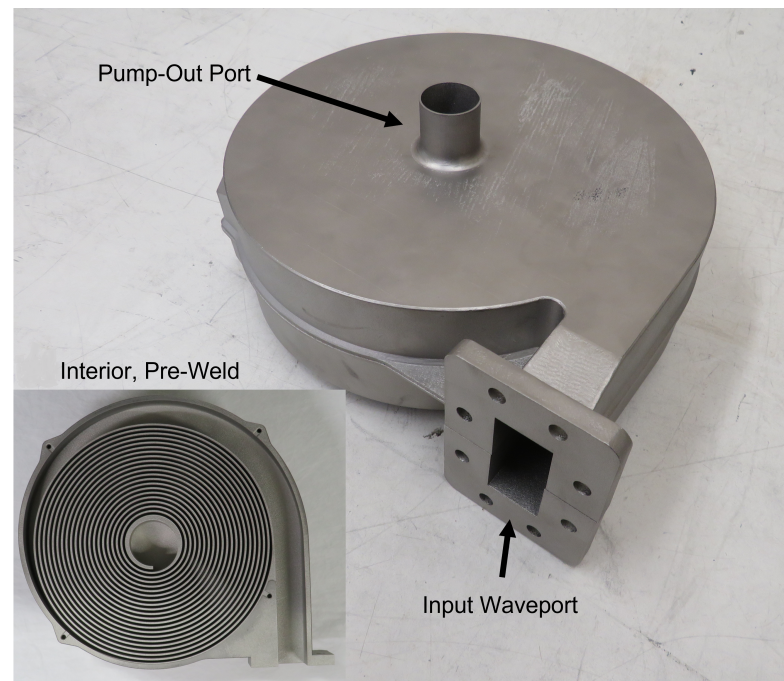


**Figure 1.** Labeled image of printed spiral load, with interior structure shown in insert.

The use of both of these processes is popular, especially in the aerospace industry, which accounts for over 18% of the AM industrial applications [1]. Aerospace applications of AM have been of particular interest to researchers as there is overlap between various other applications within the aerospace industry. PBF processes are typically used for more complex geometries, whereas DED is used for generating lightweight structures and performing repairs on existing components [5]. PBF processes have also been utilized to produce lightweight antennas for small satellites, showing the overlap between aerospace and research [6]. To understand how these processes can be used to generate RF components, the DED and PBF methods must be understood.

Direct energy deposition utilizes a wire or powder feeder that allows for the stock to be melted by an energy source as the material is extruded. The energy source can be a laser, arc-welder, or electron beam, depending on the implementation chosen [7]. This method results in relatively cheap and quickly produced parts but has the limitations of low resolution and poor layer adhesion. The low resolution also inherently limits the complexity of the parts that are possible to produce [1].

Powder bed fusion, specifically a variety of the method known as direct metal laser sintering (DMLS), operates by utilizing a laser to sinter metal rather than using a laser to melt particles together that typically have a single melt temperature or are covered in a polymer binder [8]. The typical DMLS machine operates by first raising the feeder bed so that a recoater blade can push the upper layer of the metal particles to coat the build platform. Any excess powder that does not cover the build plate are pushed into an excess bin on the opposite side of the build plate from the feeder bin. A laser then sinters the particles together in the desired pattern for the given layer. The build plate then lowers, another layer of particles is coated on top of the last layer, and the process repeats until the part is finalized [9]. Figure 2 shows how these components are typically laid out. The lack of the binding polymer necessary for other powder bed fusion methods also allows for higher-resolution parts to be created [1]. Two of the major drawbacks of the DMLS method are that its cost is higher and its print times are longer compared with those of other methods [10].
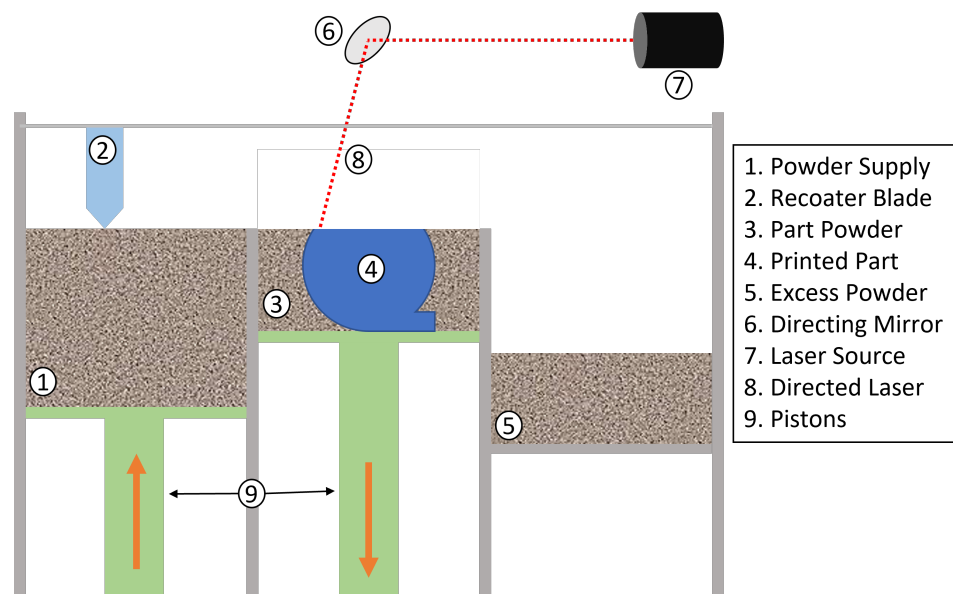
**Figure 2.** Diagram showing the common components of a DMLS machine.

During the design phase, considerations are made with regard to the general limitations of current DMLS technologies and how AM processes affect the printed design. A factor driving the solid model design due to the AM process is the issue of internal support materials. Internal support material may be added in the event an internal cavity has an excessive overhang due to the layer-by-layer nature of AM [11]. Unlike external support material, internal supports are impractical if not impossible to remove once they are printed, causing unexpected performance compared with simulations.

While limitations with DMLS exist, these limitations are reflected in most of the other forms of additive manufacturing. DMLS also provides many advantages, as previously mentioned, that favor its use over others methods such as DED. These advantages have led to PBF methods being more commercially prevalent than DED methods, making it easier to find companies that provide AM services via PBF methods [12]. Furthermore, these identified drawbacks have been mitigated through implementable design principles.

*1.2. Motivation*

Previous research has been performed on the use of AM to develop components for accelerator concepts. Of particular interest have been interim reports from research performed by CERN demonstrating the way in which different materials and designs affect the performance of AM X-band load structures. This research showed promising results within the X-band range, with simulations showing the optimized waveguide geometry in Ti-6Al-4V being $-39.07$ dB in the $S_{11}$ at a frequency of 11.9942 GHz [4]. Several variations of the design have been produced using different metals such as Ti-6Al-4V and 316L stainless steel. Of the eight models produced in preliminary findings, two of them were manufactured with 316L stainless steel and performed around $-20$ dB in the $S_{11}$ at 11.9942 GHz [13]. These results showed the potential for further development in the utilization of this method for use within future collider and accelerator concepts.

The Cool Copper Collider ($C^3$) is a proposed lepton-collider Higgs factory [14,15] which has a planned center C-band frequency of 5.712 GHz [16]. By using C band instead of the more traditional S and UHF bands seen in many high energy colliders currently, it greatly reduces the necessary size to obtain TeV-scale accelerators [17]. By utilizing additive manufacturing in the production process, it will allow for rapid and flexible manufacturing of the large number of terminating loads that will be necessary for such a collider.

Proto Labs Inc., Maple Plain, MN, USA, a third-party prototype manufacturing company, was used for the fabrication of the MAM parts of the load to demonstrate the practicality of using standard manufacturing pipelines for the creation of high-power RF

components. As DMLS machines are expensive to procure and require additional time and money for maintenance, using a third-party company with DMLS as part of their standard offerings greatly reduced the barrier to entry for the research performed. The company specifies that they are able to provide a resolution of 30 microns with tolerances of 0.076 mm $\pm$ 1% of the nominal length [9]. Proto Labs is able to ensure the quality of the parts produced by performing standard heat treatment per ASTM 3301 and testing sample mechanical properties and density per ASTM E8 and B311 standards, respectively [18].

## 2. Methodology

The design for the load structure was based on the limitations of the chosen manufacturing method and two main design principles. DMLS is a flexible process, but is mainly limited by the necessity of support material and the size of the build platform. These limitations had to be considered throughout the design process. The first design principle that was implemented was designing the entire assembly to be produced on a standard DMLS machine. This limited the necessity to consider components that might complicate the design through interfacing between additive and traditionally machined components. The second design principle was ensuring that the designed load was broadband. This meant that there would be no resonant structures, which typically require more precise control of the surface imperfections.

All simulations were performed using Ansys High-Frequency Structure Simulator (HFSS) software 2022 R1. Simulations were performed to observe the effects of the change in each major component of the design (taper, spiral, pump-out hardware) on the overall performance. Initial designs were based off of those conducted in the X-band [4] and modified to better match the frequency range of the C band. The goal of these models was to achieve an $S_{11}$ value of $-20$ dB or lower at 5.712 GHz with a wide bandwidth. The bandwidth was necessary to avoid problems due to the manufacturing and tuning of the structure. The initial model generated was a straight-line, nonstandard waveguide without any taper to a standard WR-187 waveguide. This was selected to ensure that the nonstandard waveguide model allowed for broadband transmission of an arbitrary signal around the C-band range.

Tapers were used to transition from the standard WR-187 waveport to the nonstandard waveguide. Two different tapers were tested in the height dimension: a linear taper and a sinusoidal taper. A simple linear expansion from the narrower port width to the wider waveguide width was designed. Equation (1) defines the sinusoidal profile using the given variables from Table 1 to show both the linear and sinusoidal taper in Figure 3a.

**Table 1.** Definitions of variables labeled in Figure 3a.

| Variable Name | Symbol | Value (mm) |
| --- | --- | --- |
| Port Width | $w_{wr}$ | 47.55 |
| Port Height | $h_{wr}$ | 22.15 |
| Waveguide Width | $w_{wg}$ | 60 |
| Waveguide Height | $h_{wg}$ | 2 |
| Taper Length | $l_t$ | 400 |
| Waveguide Length | $l_{wg}$ | 7000 |

$$x(z) = \frac{h_{wr} + h_{wg}}{2} + \frac{h_{wr} - h_{wg}}{2} \cos(\frac{\pi}{l_t} z) \, , \; z \in (0, l_t) \tag{1}$$

Once the models for the straight waveguide without any taper and the two with the linear and sinusoidal tapers were developed, models for their spiraled versions were generated. The straight portion of the waveguide was modeled with sweeping a rectangular face along a line defined by (2). Following the spiral equation of the straight waveguide, equations were developed for the two taper versions. The interior face of each taper was curved around the inner spirals along the line defined by (2) to match the straight models. The outer faces of the tapers were separately defined to maintain similar behavior to the

straight-line model. Equation (4) shows the modified version of the linear taper in the spiral form, and (6) shows the modified version of (1) in the spiral form.

$$\begin{cases} x(t) = (R + \alpha t)\sin(2\pi t) \\ y(t) = (R + \alpha t)\cos(2\pi t) \end{cases} \quad t \in (0, t_l) \tag{2}$$

$$\alpha = h_{wg} + g \tag{3}$$

$$\begin{cases} x(t) = (R + h_{wg} + (\alpha + \beta)t)\sin(2\pi t) \\ y(t) = (R + h_{wg} + (\alpha + \beta)t)\cos(2\pi t) \end{cases} \quad t \in (0, t_t) \tag{4}$$

$$\beta = \frac{h_{wr} - h_{wg}}{t_t} \tag{5}$$

$$\begin{cases} x(t) = (R + h_{wg} + \kappa(t)\frac{t}{t_t})\sin(2\pi t) \\ y(t) = (R + h_{wg} + \kappa(t)\frac{t}{t_t})\cos(2\pi t) \end{cases} \quad t \in (0, t_t) \tag{6}$$

$$\kappa(t) = \left(\frac{h_{wg} - h_{wr}}{2}\right)\cos\left(\pi\frac{t}{t_t}\right) + \frac{h_{wg}}{4} + \frac{h_{wr}}{2} + gt_t \tag{7}$$

Equations (4)–(7) define the x and y coordinates that define the lines at $z(t) = 0$, but we must add (8) to add the width taper to the sinusoidal and linear height taper

$$z(t) = \frac{w_{wg}}{2} - \left(\frac{w_{wg} - w_{wr}}{2t_t}\right)t. \tag{8}$$

Figure 3b shows how the various parameters of the spiral waveguide model were defined within HFSS. These values were modified slightly throughout the initial simulation runs to optimize the load performance. Table 2, $w_{wg}$, and $h_{wg}$ from Table 1 define the parameters that were found to balance performance and printability of the spiral load structure.



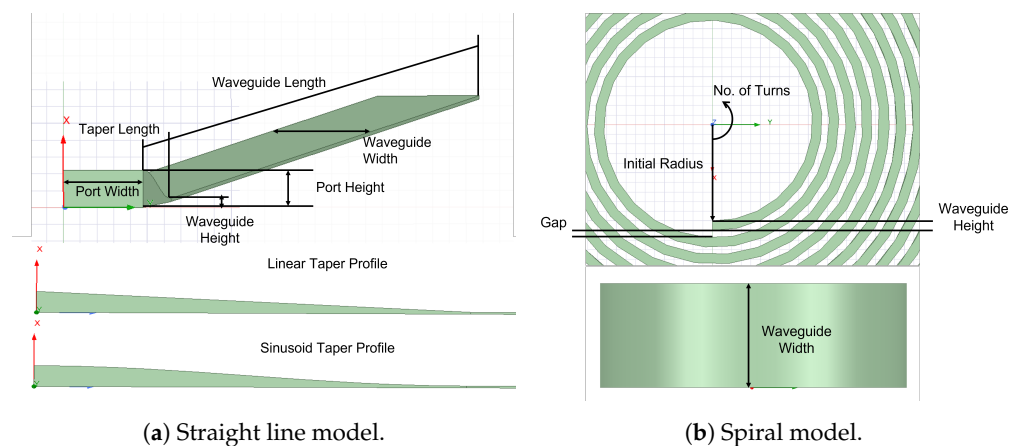(**a**) Straight line model.    (**b**) Spiral model.

**Figure 3.** Diagrams of initial models used for simulations. The variables used to define the dimensions labeled can be found in Tables 1 and 2.

**Table 2.** Definitions of variables labeled in Figure 3b.

| Variable Name | Symbol | Value | Units |
|---|---|---|---|
| Gap | $g$ | 1.5 | mm |
| Initial Radius | $R$ | 20 | mm |
| No. of Turns | $t_l$ | 19.5 | rev |
| Taper Turn Length | $t_t$ | 0.75 | rev |

The last development step of the model was to add the pump-out hardware into the vacuum space model. This was an important step as it allowed the results of the simulation to more closely match the real-world performance of the load. It also had to accommodate the need to remove powder from the interior of the load after the printing process. The model shown in Figure 4 includes the pump-out volume and WR-187 extension so that there was room for a flange to be added. The design shown also minimizes the inherent reflections caused by the slits and allows for the model to be split in two so that the final printed model is rendered in two halves. This allows for issues related to internal support material and powder removal to be mitigated.
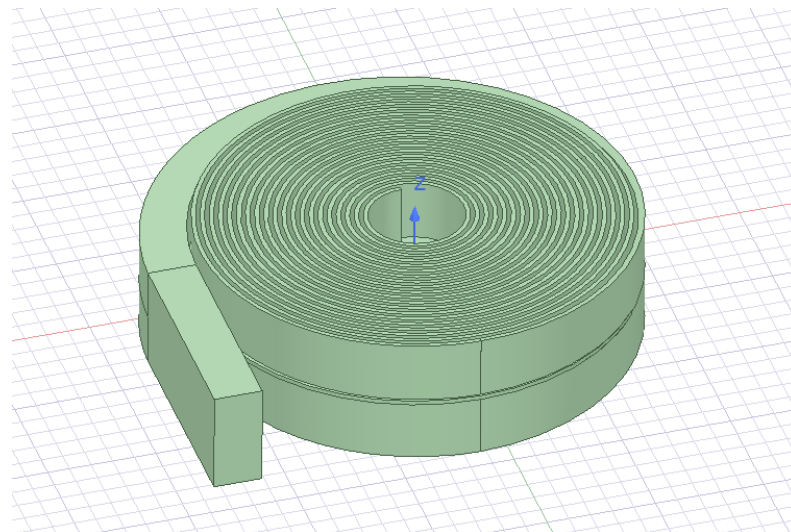


**Figure 4.** Final spiral load vacuum model and pump-out slits within HFSS simulation software.

### 3. Results

*3.1. Simulation Results*

Using the straight waveguide model without any taper to a WR-187 port, it was then possible to compare the performance of the two different taper designs and dimensions described in the Methodology section. The addition of these tapers to the model and its comparison to the simulation run without the taper are shown in Figure 5a. This plot shows that there was very little difference between the two taper designs in the straight load model. It showed slightly worse performance in the $S_{11}$ data when the taper was added when observing the changes at the desired center frequency of the load. This was expected to occur and could be explained by the additional reflections caused by the taper geometries. This was mainly due to the impedance mismatch from one side to another. It required further investigation into the potential effects that the tapers would have once the model was moved from a straight model to a spiral model to make a determination on what taper to utilize in the design.

Adding the effect of the spiral load led to the ability to differentiate the effects of the sinusoidal taper and the linear taper. Figure 5b shows a plot of these differences. The sinusoidal taper produced an $S_{11}$ value of −21.7 dB at the desired frequency of 5.712 GHz. It performed better than the linear taper method (−19.5 dB) and similar to if had there been no taper method utilized (−21.9 dB). For these reasons, it was decided to move on with the

sinusoidal taper method in future simulation models as it showed better performance than the linear taper in the $S_{11}$ plot.
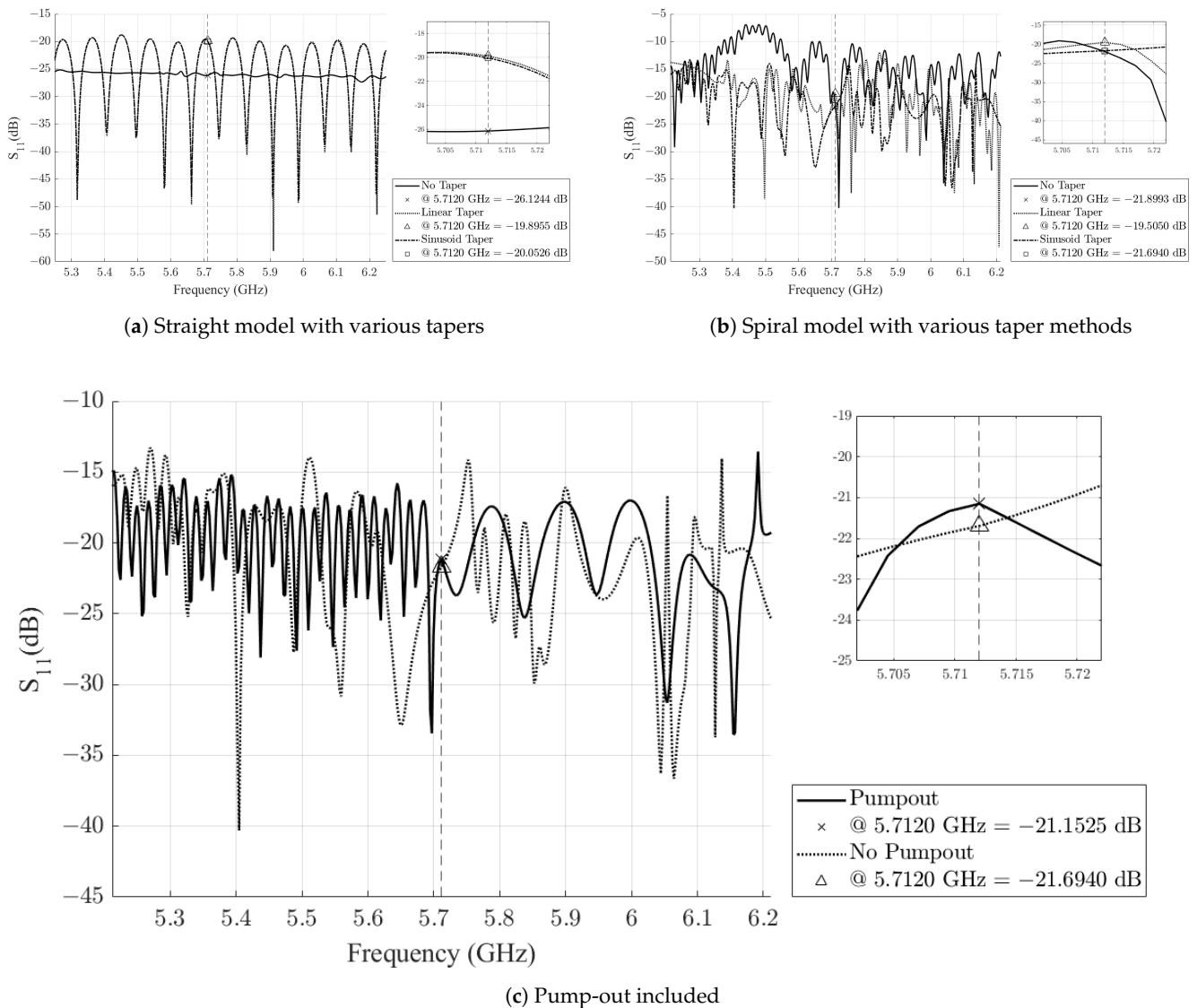


(**a**) Straight model with various tapers



(**b**) Spiral model with various taper methods



(**c**) Pump-out included

**Figure 5.** Plots of the $S_{11}$ values generated by comparing the results of various simulated models.

Following the use of the spiral load model, the final pump-out model with all of the additional vacuum space designed for pump-out could be simulated. This was performed to show the potential effects of the additional pump-out model on the reflections. This difference between the non-pump-out spiral model and the model that added the pump-out hardware can be seen in Figure 5c. The plot shows a slight variation in the $S_{11}$ data across the frequency sweep. At the desired frequency of 5.712 GHz, the plots show a close match, with the pump-out model showing an $S_{11}$ value of $-21.2$ dB and the model without showing a response of $-21.7$ dB. This shows that the designed pump-out does not have a significant negative impact to the performance of the spiral load.

*3.2. Printed Model Results*

Before the welding of the two halves of the spiral load, a cold test was performed for initial validations of the simulations and to verify that there were no unexpected results due to the printing process. The data for all of the cold tests were recorded on an Agilent N5241A vector network analyzer (VNA), which was calibrated using the thru, line, reflect

(TLR) calibration method. The initial cold test was performed by inserting the alignment pins and clamping the two halves of the spiral load together. The spiral load was then connected to the VNA, a photograph of which can be seen in Figure 6a. The results from this initial cold test, before any welding or machining occurred, can be seen in Figure 7a.



(**a**) Initial preweld setup            (**b**) Vacuum setup

**Figure 6.** Images showing the setup of the spiral load under various conditions.

These results were promising, with the initial cold test showing that at a frequency of 5.712 GHz, the load was able to perform much better than expected according to simulations with an $S_{11}$ value of $-38.7$ dB. This result at the specific frequency was due to the fringing response being shifted, and the overall power absorption was more consistent with the simulations. Following the initial cold test, the two halves were welded together, and the instrumentation flange was kept to perform further tests on the load. Welding the two halves together had a significant effect on the $S_{11}$ curve, as shown in Figure 7b. This resulted in an $S_{11}$ value of $-26.8$ dB. While this was a significant difference at the specific frequency, the overall power absorption across the spectrum was consistent.

So that the same printed load was used throughout all tests performed, the spiral load underwent a process of removing the instrumentation flange, and high-vacuum interfaces were added. Following this process, the spiral load was cold tested again under atmospheric conditions to see if there was any shift in the response due to the additional welding and brazing processes. Figure 7c shows the plot that resulted from this process under atmospheric conditions. It can be seen that at the center frequency of 5.712 GHz, the $S_{11}$ value shifted up slightly from that of the previous cold test to a value of $-25.1$ dB. The load was then attached to a vacuum pump, and an RF window was used to test the response while under vacuum conditions. A photograph of the bench setup is shown in Figure 6b, and the results of the test are shown in Figure 7d. Adding the RF window and pumping the spiral load down to vacuum decreased the performance slightly to an $S_{11}$ value of $-22.8$ dB at the center frequency of 5.712 GHz.

The spiral load was sent to Radiabeam following all of the cold tests performed at SLAC to observe how the spiral load would perform while under high-power loading. The load was first conditioned to prevent breakdown and damage to the spiral load structure. Conditioning began with a 200 ns pulse width at 47 kW of power, with a repetition rate of 1 Hz. The power and repetition rate were then gradually stepped up to a rate of 20 Hz and maximum power of 8 MW. The pulse width was then increased once the load had been conditioned at the 200 ns pulse width to a pulse width of 400, 700, and finally 1000 ns. Once the load had been conditioned, the load was able to terminate a peak power of 8.1 MW with a repetition rate of 20 Hz when the pulse width was set to 700 ns. Figure 8 shows the forward and reflected signal from the load during testing.
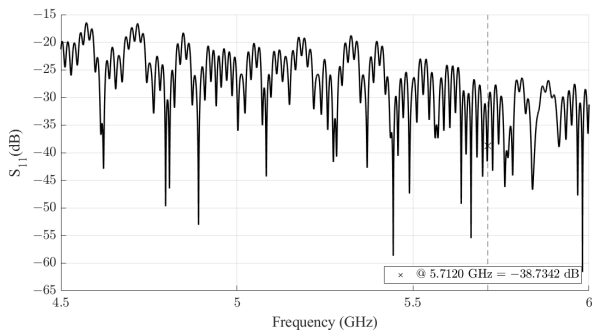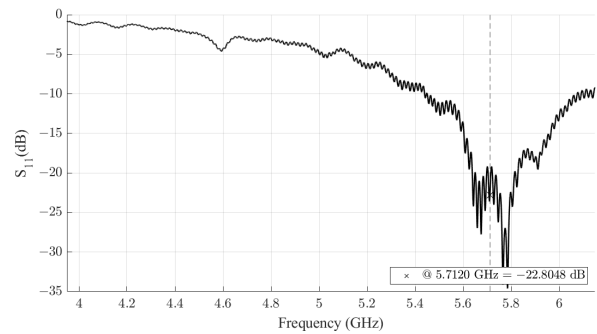
(**a**) Initial cold test.
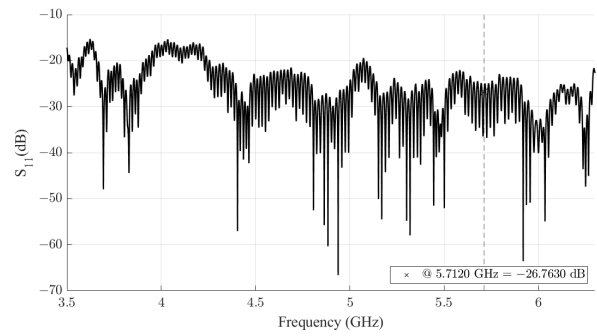


(**b**) Post-weld.
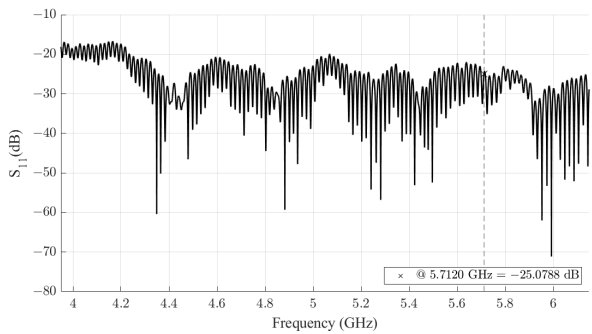


(**c**) Vacuum hardware added, under atmospheric conditions.



(**d**) Vacuum hardware added, under vacuum.

**Figure 7.** Measured $S_{11}$ values of the realized load structure while under various stages of development and atmospheric conditions. Figure 7d has a smaller bandwidth of attenuation due to the limited bandwidth of the RF window used during testing.
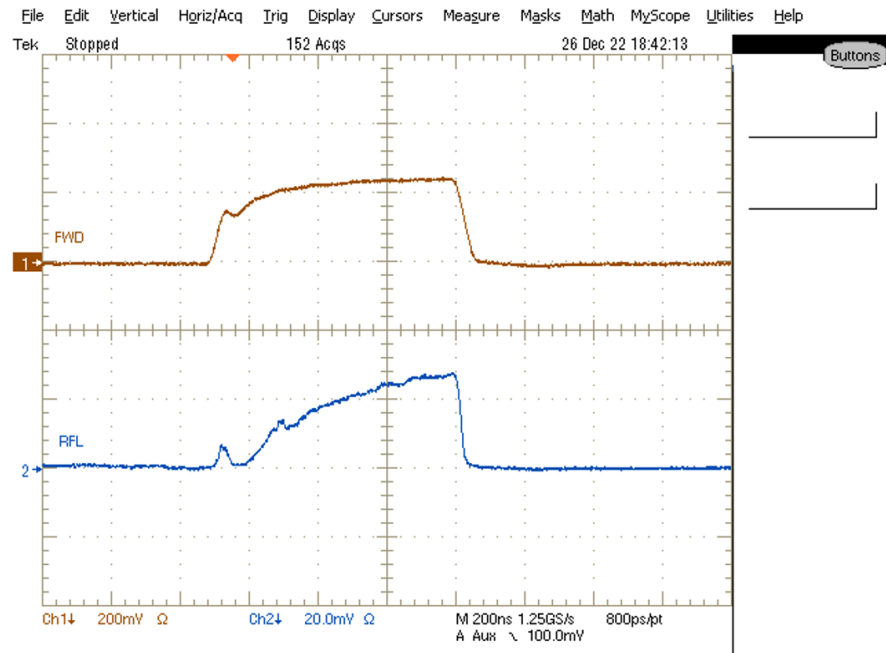


**Figure 8.** Screen capture of oscilloscope during testing with 8.1 MW power input at a 20 Hz repetition rate and 700 ns pulse width.

During the high-power testing, the vacuum was able to stay stable at $3 \times 10^{-7}$ Torr when under a pulse width of 400 ns. The temperature of the spiral load, as measured with a thermocouple attached to the exterior of the load, showed an increase from 22.8 °C to

27.9 °C over the testing period. When the load was tested with the 1000 ns pulse width, heating increased significantly. A peak temperature of 43.5 °C was present on the exterior of the load, and the vacuum increased from nominal at $3 \times 10^{-7}$ Torr to $1.3 \times 10^{-6}$ Torr, causing testing at the 1000 ns pulse width to be paused. As the load was only passively cooled by the ambient atmosphere, a cooling fan was added and assisted in bringing down the peak temperatures to 34.9 °C and stabilized the pressure to $5.6 \times 10^{-7}$ Torr.

## 4. Discussion

The results show the feasibility of utilizing additive manufacturing to produce high-power C-band load structures. Using simulations in the initial development of the spiral load assisted with the development of an operational solution. Two of the concerns in using simulations when compared with the manufactured model are the effect of slight misalignment (<0.1 mm) of the two halves and the exact location and height of the surface roughness. The slight misalignment was due to slightly different shrinkage rates seen in the two halves, leading to a discontinuity in the sidewalls. The surface roughness of the interior of the load was able to be approximately, simulated but some of the regions of the load had a rougher surface than others, dependent on the angle that it was placed at within the DMLS machine. While these issues were present, it is understood that they had a neutral effect in the case of misalignment and a positive effect in the case of surface roughness.

Previous research on the use of AM to produce waveguides in the 50–110 GHz range of the RF spectrum demonstrated that the surface roughness decreases the transmission coefficient from smooth-wall simulations, with ~0.2–1 dB of additional loss measured [19,20]. These studies also showed further similarity in overall results, showing that the exact DMLS machine used has little effect on the RF performance of the produced parts. In the study by Verploegh et al. [19], a 10 cm long waveguide produced with AlSi10Mg powder showed a $S_{21}$ transmission coefficient around 2 dB (~−0.2 dB/cm). Similarly, Manafi et al. [20] utilized Proto Labs to produce double-ridge waveguides and found that the waveguides produced with aluminum powder resulted in an $S_{21}$ transmission coefficient of ~−0.25 dB/cm. More general research also supports the reliability of being able to produce components with similar surface qualities across various machines, assuming similar settings and powder are used [21].

While the load was able to terminate a peak power of 8.1 MW, testing on the load had to be stopped due to concerns over the stability of the vacuum pressure and the temperature on the external surface of the load. The increase in heat on the exterior following the finishing of testing suggested that there was a fairly significant amount of heat being produced on the interior walls of the spiral load, especially in the outer turns. This signifies that much of the power loss is concentrated in the first two or three turns of the spiral load. While it is known that the additional turns increased the overall performance, this concentration in surface loss led to uneven heating in the load and a reduction in the longevity of the performance of the load as vacuum pressure suffered. Future iterations of this design will need to include an integrated cooling system, an optimized waveguide shape to even out the surface loss concentrations, or both. These additions would allow for higher powers to be terminated, thus expanding the ability to use such processes.

This study shows the feasibility of the use of additive manufacturing techniques for the development of C-band load structures. The ability for additive manufacturing processes to adapt easily to the design needs of the finalized structure allows greater flexibility in the manufacturing process. The basic spiral load having proved the ability to perform at high powers allows for the advancement and further optimization for the specific applications of the load. The results show promise for the future use of this technique in the $C^3$ concept.

**Author Contributions:** Conceptualization, E.N., C.W. and J.M.; methodology, C.W. and J.M.; software, C.W.; validation, G.M. and J.M.; resources, G.M. and E.N.; data curation, B.S., J.M., R.A., A.D. and R.B.; writing—original draft preparation, G.M.; writing—review and editing, E.N., C.W., B.S., J.M. and G.M.; visualization, G.M.; supervision, E.N. All authors have read and agreed to the published version of the manuscript.

**Data Availability Statement:** The data presented in this study are available on request from the corresponding author.

**Conflicts of Interest:** The authors declare no conflict of interest.

## References

1. Ngo, T.D.; Kashani, A.; Imbalzano, G.; Nguyen, K.T.; Hui, D. Additive manufacturing (3D printing): A review of materials, methods, applications and challenges. *Compos. Part B Eng.* **2018**, *143*, 172–196. [CrossRef]
2. Zhang, B.; Guo, Y.X.; Zirath, H.; Zhang, Y.P. Investigation on 3-D-Printing Technologies for Millimeter- Wave and Terahertz Applications. *Proc. IEEE* **2017**, *105*, 723–736. [CrossRef]
3. Wehner, C.; Merrick, J.; Shirley, B.; Weatherford, B.; Mathesen, G.; Nanni, E. RF Properties and Their Variations in a 3D Printed Klystron Circuit and Cavities. *arXiv* **2022**, arXiv:2211.15500.
4. Bursali, H. X-Band Spiral Load RF Design. 2020. Available online: https://edms.cern.ch/document/2404437/1 (accessed on 8 January 2021).
5. Mohd Yusuf, S.; Cutler, S.; Gao, N. Review: The Impact of Metal Additive Manufacturing on the Aerospace Industry. *Metals* **2019**, *9*, 1286. [CrossRef]
6. Chio, T.H.; Huang, G.L.; Zhou, S.G. Application of Direct Metal Laser Sintering to Waveguide-Based Passive Microwave Components, Antennas, and Antenna Arrays. *Proc. IEEE* **2017**, *105*, 632–644. [CrossRef]
7. Svetlizky, D.; Das, M.; Zheng, B.; Vyatskikh, A.L.; Bose, S.; Bandyopadhyay, A.; Schoenung, J.M.; Lavernia, E.J.; Eliaz, N. Directed energy deposition (DED) additive manufacturing: Physical characteristics, defects, challenges and applications. *Mater. Today* **2021**, *49*, 271–295. [CrossRef]
8. Nancharaiah, T. A review paper on metal 3d Printing Technology. In *Advances in Materials Processing and Manufacturing Applications: Proceedings of the iCADMA 2020, Jaipur, India, 5–6 November 2020*; Springer: Singapore, 2021; pp. 251–259. [CrossRef]
9. Protolabs. Metal 3D Printing Service. Available online: https://www.protolabs.com/services/3d-printing/direct-metal-laser-sintering/ (accessed on 20 June 2023).
10. Franco, D.; Miller Devós Ganga, G.; de Santa-Eulalia, L.A.; Godinho Filho, M. Consolidated and inconclusive effects of additive manufacturing adoption: A systematic literature review. *Comput. Ind. Eng.* **2020**, *148*, 106713. [CrossRef]
11. Davis, T. A deep dive into metal 3D printing. In Proceedings of the Laser 3D Manufacturing VI, San Francisco, CA, USA, 2–7 February 2019; Gu, B., Helvajian, H., Chen, H., Eds.; SPIE: Bellingham, WA, USA, 2019; Volume 10909, p. 1090907. [CrossRef]
12. Cherdo, L. Metal 3D Printers in 2023: A Comprehensive Guide. 2022. Available online: https://www.aniwaa.com/buyers-guide/3d-printers/best-metal-3d-printer/ (accessed on 9 August 2023).
13. Bursali, H. Spiral Loads RF Measurement. 2020. Available online: https://edms.cern.ch/document/2323664/1 (accessed on 28 July 2022).
14. Bai, M.; Barklow, T.; Bartoldus, R.; Breidenbach, M.; Grenier, P.; Huang, Z.; Kagan, M.; Lewellen, J.; Li, Z.; Markiewicz, T.W.; et al. C$^3$: A "Cool" Route to the Higgs Boson and Beyond. *arXiv* **2021**, arXiv:2110.15800.
15. Dasu, S.; Nanni, E.A.; Peskin, M.E.; Vernieri, C.; Barklow, T.; Bartoldus, R.; Bhat, P.C.; Black, K.; Brau, J.; Breidenbach, M.; et al. Strategy for understanding the Higgs physics: The cool copper collider. *arXiv* **2022**, arXiv:2203.07646.
16. Nanni, E.A.; Breidenbach, M.; Vernieri, C.; Belomestnykh, S.; Bhat, P.; Nagaitsev, S.; Bai, M.; Berg, W.; Barklow, T.; Byrd, J.; et al. C$^3$ Demonstration Research and Development Plan. *arXiv* **2022**, arXiv:2203.09076.
17. Bane, K.L.; Barklow, T.L.; Breidenbach, M.; Burkhart, C.P.; Fauve, E.A.; Gold, A.R.; Heloin, V.; Li, Z.; Nanni, E.A.; Nasr, M.; et al. An Advanced NCRF Linac Concept for a High Energy e$^+$ e$^-$ Linear Collider. *arXiv* **2018**, arXiv:1807.10195.
18. Protolabs. Designing for Metal 3D Printing. 2019. Available online: https://www.protolabs.com/media/1020535/protolabs_dmls_design_guide.pdf (accessed on 8 August 2023).
19. Verploegh, S.; Coffey, M.; Grossman, E.; Popović, Z. Properties of 50–110-GHz Waveguide Components Fabricated by Metal Additive Manufacturing. *IEEE Trans. Microw. Theory Tech.* **2017**, *65*, 5144–5153. [CrossRef]
20. Manafi, S.; Al-Tarifi, M.; Filipovic, D.S. Millimeter-Wave Double-Ridge Waveguide and Components. *IEEE Trans. Microw. Theory Tech.* **2018**, *66*, 4726–4736. [CrossRef]
21. Gallant, L.; Hsiao, A.; Mcsorley, G. Benchmark Physical And Mechanical Property Characterization Of 316L Stainless Steel DMLS Prints. In Proceedings of the Canadian Society for Mechanical Engineering International Congress 2021, Charlottetown, PE, Canada, 27–30 June 2021. [CrossRef]